



# Mechanical properties of AlCoCrCuFeNi high-entropy alloys using molecular dynamics and machine learning



Hoang-Giang Nguyen <sup>a,d</sup>, Thanh-Dung Le <sup>b,f</sup>, Hong-Giang Nguyen <sup>c</sup>, Te-Hua Fang <sup>a,e,\*</sup>

<sup>a</sup> Department of Mechanical Engineering, National Kaohsiung University of Science and Technology, Kaohsiung 807, Taiwan

<sup>b</sup> Department of Electrical Engineering, École de Technologie Supérieure, University of Québec, Montréal, Québec, Canada

<sup>c</sup> Institute of Testing and Quality Assurance in Education, Hue University, Hue City 49000, Viet Nam

<sup>d</sup> Faculty of Engineering and Technology, Kien Giang University, Kien Giang Province, Viet Nam

<sup>e</sup> Department of Fragrance and Cosmetic Science, Kaohsiung Medical University, Kaohsiung 807, Taiwan

<sup>f</sup> Interdisciplinary Centre for Security, Reliability, and Trust (SnT), University of Luxembourg

## ARTICLE INFO

### Keywords:

High-entropy alloys  
Molecular dynamics  
Machine learning  
Tensile stress  
Long Short-Term Memory

## ABSTRACT

High-entropy alloys (HEAs) stand out from multi-component alloys due to their attractive microstructures and mechanical properties. In this investigation, molecular dynamics (MD) simulation and machine learning (ML) were used to ascertain the deformation mechanism of AlCoCrCuFeNi HEAs under the influence of temperature, strain rate, and grain sizes. First, the MD simulation shows that the yield stress decreases significantly as the strain and temperature increase. In other cases, changes in strain rate and grain size have less effect on mechanical properties than changes in strain and temperature. The alloys exhibited superplastic behavior under all test conditions. The deformity mechanism discloses that strain and temperature are the main sources of beginning strain, and the shear bands move along the uniaxial tensile axis inside the workpiece. Furthermore, the fast phase shift of inclusion under mild strain indicates the relative instability of the inclusion phase of hexagonal close-packed (HCP). Ultimately, the dislocation evolution mechanism shows that the dislocations are transported to free surfaces under increased strain when they nucleate around the grain boundary. Surprisingly, the ML prediction results also confirm the same characteristics as those confirmed from the MD simulation. Hence, the combination of MD and ML reinforces the confidence in the findings of mechanical characteristics of HEA. Consequently, this combination fills the gaps between MD and ML, which can significantly save time, human power, and cost to conduct real experiments for testing HEA deformation in practice.

## 1. Introduction

Molecular dynamics (MD) is a simulation method that examines the real-time movements of atoms and molecules within N-body system [1–3]. It computes the paths of these particles through resolving the motion equations of Newton [4,5]. MD is used to get fundamental insights into the deformation mechanisms of metals and alloys [6–13]. High entropy alloys (HEA) represent a unique and attractive group of multi-component alloys comprising more than four primary elements in varying atomic percentages [14–18]. One of the HEAs that has been extensively studied for its outstanding mechanical properties is  $\text{Al}_x\text{Cr-CoFeCuNi}$ , with  $x$  (the molar ratio in the alloy) ranging from 0 to 3 [19–30].

The AlCoCrCuFeNi HEA is one of the most well-known and

extensively researched HEAs; studies have focused on phase creation, mechanical characteristics, and microstructure [31–33]. Fang et al. [34] investigated the deformation characteristics of a  $\text{Cu}_{29}\text{Zr}_{32}\text{Ti}_{15}\text{Al}_5\text{Ni}_{19}$  high entropy bulk metallic glass (HE-BMG) under nanoindentation conditions employing extensive molecular dynamics simulations at a large scale. Li et al. [35] investigated the tensile deformation behavior of an FCC-structured  $\text{Fe}_{45}\text{Co}_{25}\text{Ni}_{10}\text{V}_{20}$  high-entropy alloy at cryogenic temperatures. The alloy exhibited remarkable mechanical properties, including a tensile strength of 1.1 GPa, an ultrahigh fracture elongation of 82 %, and a minimal strain hardening rate at a true strain of approximately 40 %. These findings contribute to elucidating the significance of transformation-induced plasticity effects on the cryogenic properties of alloys. Wang et al. [36] fabricated a set of non-equiautomic ( $\text{Co}_{40}\text{Fe}_{25}\text{Cr}_{20}\text{Ni}_{15}\text{Al}_5$ ) HEA through flash electro-pulsing annealing at

\* Corresponding author at: Department of Mechanical Engineering, National Kaohsiung University of Science and Technology, Kaohsiung 807, Taiwan.  
E-mail address: [fang@nkust.edu.tw](mailto:fang@nkust.edu.tw) (T.-H. Fang).

different voltages, combined with deformation twinning during plastic deformation. Their results outline a successful approach for adjusting the mechanical characteristics of HEAs through modulation of the annealing voltage. Li et al. [37] synthesized Co-rich ( $\text{Co}_{40}\text{Fe}_{25}\text{Cr}_{20}\text{Ni}_{15}$ ) $_{100-x}\text{Al}_x$  ( $x = 0$  and  $5$  at%) HEA and evaluated their tensile properties at room temperature. Intriguingly, both alloys exhibited deformation via mechanical twinning, as evidenced by MD simulations. These results offer insights into the role of aluminum alloying in governing the mechanical behavior of HEAs. The number of related studies has expanded recently due to the development of a newly designed AlCoCrCuFeNi HEA founded on optimizing structural performance [38].

To fully comprehend the deformation mechanism of the material, it is imperative to take into account the presence of the hexagonal close-packed (HCP) phase in the substrate from the outset. The HCP phase typically arises inside the crystal structure during the deformation of the material. Defects typically manifest during processes like tension, compression, indentation, imprinting, and cutting of materials. Several research studies have investigated the influence of temperature or strain rate on the mechanical characteristics of materials [39,40]. MD simulations have been essential in improving our understanding of deformation, phase transitions, and stress, particularly at the nanoscale, when used in conjunction with experimental studies. This is important since it is difficult for experiments to thoroughly explore material phenomena at this scale [41,42].

Several studies have employed ML alongside molecular and materials modeling in previous research. For instance, Keith et al. [43] explored various cases in which computational chemistry and machine learning collaborate to offer valuable predictions in molecular and materials modeling, retrosyntheses, catalysis, and drug discovery. Mayer et al. [44] introduced the concept of homogeneous dislocation nucleation, positing the initiation of plasticity in face-centered cubic (FCC) single crystals through an analysis of elastic material characteristics. Zhang et al. [45] employed various multi-scale simulation techniques, including density functional theory (DFT) calculation and molecular dynamics method, to design high-entropy alloys and predict their properties. Utilizing molecular dynamics simulations, these findings were then translated through artificial neural networks (ANNs). While ANNs are proficient tools for discerning intricate and less apparent relationships, their application in extrapolating data necessitates caution. Their results provide supplementary materials comprising trained ANNs parameters and structural descriptions, offering flexibility for integration into the nucleation model or standalone utilization. To the best of our knowledge, there has yet to be an atomic-scale exploration of the tensile behavior of AlCoCrCuFeNi alloys, considering different temperatures, strain rates, and grain sizes, aiming to predict outcomes using machine learning. Understanding the effect of temperature, strain rate, and grain size on mechanical properties and deformation mechanisms requires a comprehensive investigation of these alloys under varied conditions. This study utilizes MD simulations on AlCoCrCuFeNi alloys with FCC structures to examine their behavior under uniaxial tensile stress at different temperatures, strain rates, and grain sizes. We explore how temperatures, strain rates, and grain sizes impact the deformation mechanism of polycrystalline AlCoCrCuFeNi HEA using MD simulation and machine learning support.

Technically, firstly, we will conduct the MD simulation to obtain the atomic models of this AlCoCrCuFeNi HEA, including assigning grain coloring, designing the workpiece, and changing the polycrystalline structures. Hence, we will get the simulation results for the mechanical properties of AlCoCrCuFeNi HEA from the MD simulation under the effect of different scenarios of grain size, temperature, and strain rate changes. Those simulation results will be compared with existing studies (simulation and experiments), and then those results will be evaluated and concluded as complying with the theory before we move to the next step.

Secondly, from the validated simulation results from the MD step, we will continue to adapt the ML algorithm to predict the strain

deformation of the AlCoCrCuFeNi HEA under the different mechanical setups. Specifically, we experiment with 6 different ML algorithms. Then, evaluate the best ML predictive model based on the evaluation metrics, including Mean Absolute Percentage Error (MAPE), Mean Absolute Error (MAE), Root Mean Square Error (RMSE), and R-Square ( $R^2$ ). We also analyze the important of each material character as the contribution to the strain deformation.

Consequently, by the combination of MD and ML, the study unveils the tensile properties of the deformation mechanism in AlCoCrCuFeNi HEA, determining its dependence on various conditions. These findings contribute to a deeper comprehension of the mechanical properties of AlCoCrCuFeNi HEA.

## 2. Materials and methodologies

### 2.1. MD simulation and model

We subjected the workpiece to uniaxial tensile loading, as depicted in Fig. 1, to reveal the plastic deformation mechanism and mechanical properties of AlCoCrCuFeNi HEA. The results from this dataset are then analyzed. The dimensions of the samples are  $300 \times 75 \times 75 \text{ \AA}^3$  ( $L \times W \times H$ ), and their total atomic count ranges from 146,117 to 146,315 atoms. In the simulated three-dimensional FCC crystal structure, atoms are positioned randomly with displacement coordinates in x, y, and z. The workpiece is aligned in three distinct directions: [1 0 0] along the X-axis, [0 1 0] along the Y-axis, and [0 0 1] along the Z-axis. The elemental chemical compositions, in atomic percent, are approximately 2 % Al, 9 % Co, 32 % Cr, 39 % Cu, 12 % Fe, and 6 % Ni [22,45,46].

The three directions all made use of periodic boundary conditions to establish stable specimen configurations before the process of tensile loading. The conjugate gradient algorithm method achieves samples in a condition of minimal equilibrium energy. Subsequently, samples are equilibrated thermodynamically for 100 picoseconds at ambient temperature and zero pressure using the isothermal-isobaric (NPT) ensemble [47,48]. The velocity-Verlet algorithm is selected with a time step of 2 fs to integrate the motion equation [49,50]. In this study, temperature and pressure are regulated during the tensile process by the Nosé-Hoover thermostat and barostat [51,52]. Table 1 provides details on the parameters and samples utilized in this investigation. Selecting a trustworthy measure of potential between atoms is essential for obtaining accurate results in MD simulations. Consequently, in order to characterize to explore interatomic interactions among Al, Co, Cr, Cu, Fe, and Ni, we utilized the embedded atom method (EAM) potential [53,54].

The effectiveness of EAM potentials has been proven in numerous prior studies involving diverse test processes [54]. The total energy  $E_{pt}$  is represented as [55,56]:

$$E_{pt} = \sum_{i=1}^n E_i = \frac{1}{2} \sum_{i,j=1}^n \varphi_{ij}(r_{ij}) + \sum_{i=1}^n F_i(\rho_i) \quad (1)$$

The pair energy  $\varphi_{ij}$  represents the energy between atoms i and j based on their distance, while  $E_i$  denotes the atomic potential energy of atom i. The embedding energy term at atom are  $(r_{ij})$  and  $F_i(\rho_i)$  depends on the local electron density  $\rho_i$ . The local electron density ( $\rho_i$ ) can be calculated using:

$$\rho_i = \sum_{\substack{i,j=1 \\ i \neq j}}^n f_{ij}(r_{ij}) \quad (2)$$

Where,  $f_{ij}(r_{ij})$  signifies the electron density contribution from atom j to the particle i site. The EAM alloy potential model defines pair potentials as follows:

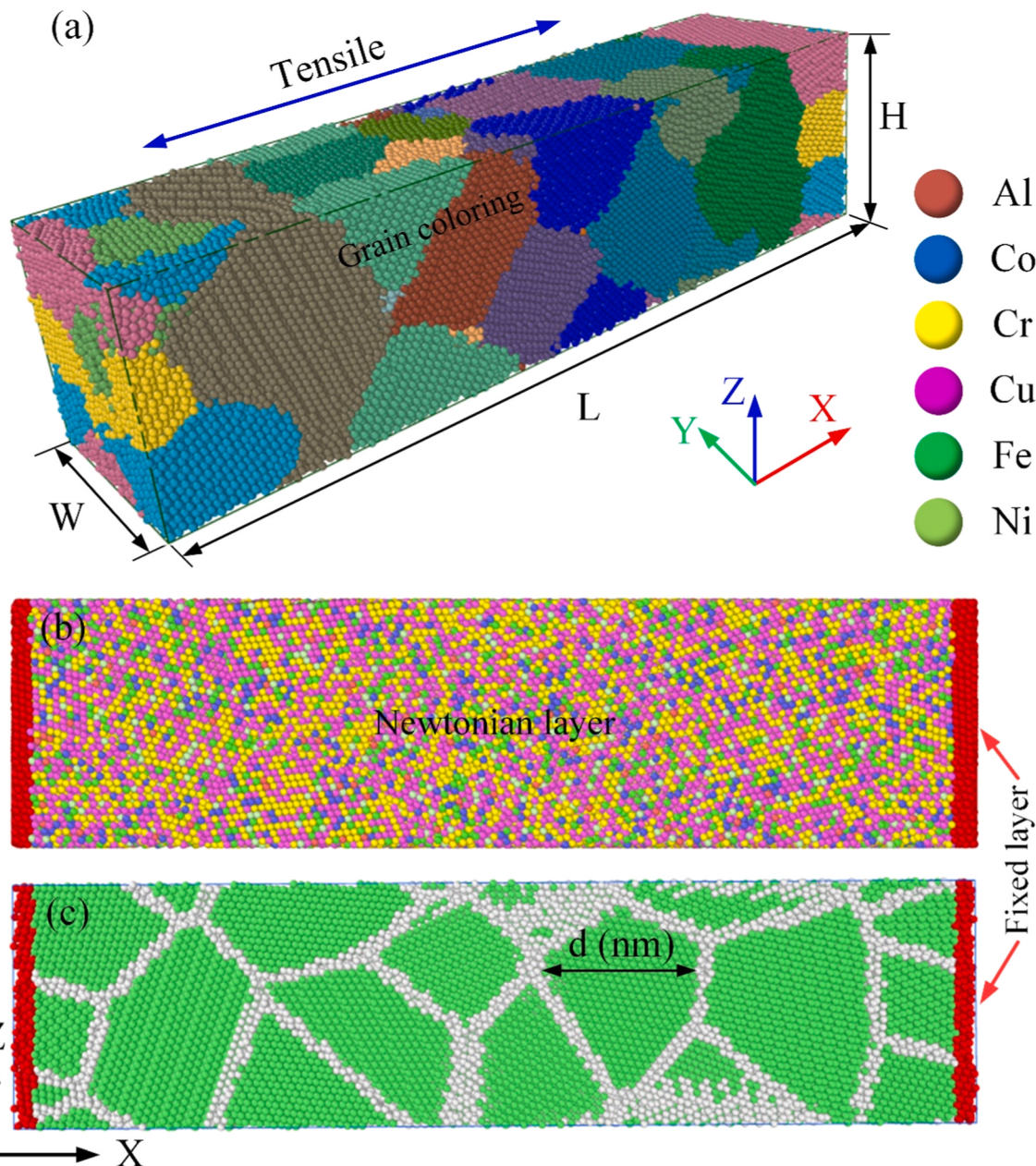


**Fig. 1.** The simulation model of AlCoCrCuFeNi HEA under tensile process.

**Table 1**  
Statistical analysis for data values.

	Strain	Temperature (K)	Grain number	Strain rate ( $\text{s}^{-1}$ )	Stress (GPa)
Count	22021	22021	22021	22021	22021
Mean	0.099997	427.2785	29.09913	$2.400064 \times 10^9$	3.345523
std	0.057791	217.8109	7.012762	$4.356896 \times 10^9$	0.901617
Min	0	300	5	$1.000000 \times 10^8$	-0.017224
25 %	0.05	300	20	$1.000000 \times 10^9$	3.961448
50 %	0.1	300	20	$1.000000 \times 10^9$	3.592606
75 %	0.15	500	20	$2.000000 \times 10^9$	3.807873
Max	0.2	1000	40	$2.000000 \times 10^{10}$	5.746938

$$\phi(r) = \frac{A \exp\left[-\alpha\left(\frac{r}{r_e}\right) - 1\right]}{1 + \left(\frac{r}{r_e} - \kappa\right)^{20}} - \frac{B \exp\left[-\beta\left(\frac{r}{r_e}\right) - 1\right]}{1 + \left(\frac{r}{r_e} - \lambda\right)^{20}} \quad (3)$$

The cutoff parameters for the electron density function are denoted as  $\kappa$  and  $\lambda$ , with adjustable parameters A, B,  $\alpha$ , and  $\beta$ . The equilibration separation between nearest neighbors is symbolized by  $r_e$ . The calculation of the electron density function mirrors the form of the attractive term in the pair potential, maintaining identical values for  $\beta$  and  $\lambda$  [56].

The density of the electron function is expressed as:

$$f(r) = \frac{f_e \exp\left[-\beta\left(\frac{r}{r_e} - 1\right)\right]}{1 + \left(\frac{r}{r_e} - \lambda\right)^{20}} \quad (4)$$

Subsequently, a pair potential is established for two different species, designated as a and b, in the following manner:

$$\phi^{nn}(r) = \frac{1}{2} \left[ \frac{f^m(r)}{f^n(r)} \phi^{nn}(r) + \frac{f^n(r)}{f^m(r)} \phi^{mm}(r) \right] \quad (5)$$

Below are the formulas [56] that define the embedding energy functions within different ranges of electron density.

$$F(\rho) = \sum_{i=0}^3 F_{ni} \left( \frac{\rho}{0.85\rho_e} - 1 \right)^i, \rho < 0.85\rho_e \quad (6)$$

$$F(\rho) = \sum_{i=0}^3 F_i \left( \frac{\rho}{\rho_e} - 1 \right)^i, 0.85\rho_e \leq \rho < 1.15\rho_e \quad (7)$$

$$F(\rho) = \sum_{i=0}^3 F_n \left[ 1 - \eta \ln\left(\frac{\rho}{\rho_s}\right) \right] \left(\frac{\rho}{\rho_s}\right)^\eta, \rho \geq 1.15\rho_e \quad (8)$$

Where  $F_{ni}$ ,  $F_i$ , and  $F_n$  are tabulated constants [53,56,57].

The Morse potential governs the remaining particle interactions [58, 59]. It is defined as follows:

$$\Phi(u_{ij}) = D [e^{-2\alpha(u_{ij}-u_0)} - 2e^{-\alpha(u_{ij}-u_0)}] \quad (9)$$

The constants for reciprocal energy and distance are represented by  $D$  and  $\alpha$ , respectively. The equilibrium and instantaneous distances during the approach of the two atoms are indicated by  $u_0$  and  $u_{ij}$ .

Estimating the average grain size, denoted as  $d$ , involves determining [60–62]:

$$d = \sqrt[3]{\frac{6V}{N}} \quad (10)$$

Where  $V$  represents the polycrystalline's overall volume of AlCoCrCu-FeNi HEA,  $N$  represents the quantity of grains. Eight workpieces with average grain sizes of 12.84, 10.19, 8.90, 8.09, 7.51, 7.07, 6.71, and 6.42 nm with grains of samples 5, 10, 15, 20, 25, 30, 35, and 40 grains, respectively, are used for this study.

In this study, analytical techniques are employed to uncover deformation behavior and structural evolution. The analysis of tensile process deformation progression is exemplified through von Mises shear strain [63]. The crystal structure, encompassing stacking defects and phase change, is examined using Honeycutt and Andersen's common neighbor analysis (CNA) method [64]. Dislocation growth during the stress process is identified using the dislocation extraction analysis (DXA) [65]. The Large-scale Atomic/Molecular Massively Parallel Simulator (LAMMPS) is employed for all simulations [58,66], while the structure is depicted and statistically analyzed using OVITO software [67].

## 2.2. Machine Learning Algorithms

### 2.2.1. Algorithms function

Machine learning allows the analysis of vast datasets through model training, facilitating tasks such as categorizing observations, identifying influential features on performance metrics, and predicting outcomes in new trials. Moreover, in fields where data-intensive techniques are uncommon, machine learning can aid researchers in designing experiments for enhanced performance or more efficient hypothesis testing. Machine learning is transforming data collection, analysis, and interpretation across various fields, including nano-optoelectronics, catalysis, and the bio-nano interface. Anticipated is the evolution of these

methodologies into discipline-specific standards, complementing the role of statistics in scientific inquiry. Nanoscience has the potential to enhance machine learning by developing electronic or photonic hardware capable of more efficient algorithm implementation than traditional computing architectures. Deepening this collaboration brings numerous benefits to both scientific communities.

This study will focus on applying machine learning techniques for predicting the stress values from the results of data from MD simulation, as shown in Fig. 5. ML for materials has been developed because of its benefits [67]. For example, superconducting material [68], which is very expensive to conduct real experiments, and extremely hard to set up and conduct the experiments.

Especially, deep learning is more advanced and robust to materials [69]. Therefore, this study will focus on different machine learning techniques for the regression model from conventional machine learning to deep learning models. Then, we can compare the effectiveness of each model based on the evaluation metrics, model complexity, and model computational resource, including:

- (1) Linear Regression (LR): Linear Regression [70] assumes a linear relationship between the input features  $x = (x_1, x_2, x_3, x_4)$ , the output  $y$ . The model predicts  $y$  using a linear function.

$$y = \beta_0 + \beta_1 x_1 + \beta_2 x_2 + \beta_3 x_3 + \beta_4 x_4 + \varepsilon \quad (11)$$

where  $\beta_0$  is the y-intercept,  $\beta_1, \dots, \beta_4$  are the coefficients for each feature, and  $\varepsilon$  is the error term

- (2) Support Vector Regression (SVR): SVR aims to find a function  $f(x)$  that deviates from  $y$  by a value no greater than  $\varepsilon$  for each training point and at the same time is as flat as possible. Mathematically, it can be represented as:

$$f(x) = w \cdot x + b \quad (12)$$

where  $w$  is the weight vector, and  $b$  is the bias. The flatness of  $f$  means minimizing  $|w|$ . This is subject to a constraint that for each  $i$ , either:

$$|y_i - f(x_i)| \leq \varepsilon \quad (13)$$

or if it is not possible, a slack variable  $\xi_i$  or  $\xi^*$   $i$  is introduced to soften the margin.

- (3) Gradient Boosting Regression (GBR): GBR [72] builds an incremental model, optimizing any differentiable loss function. At each stage, a regression tree  $h_m(x)$  is fitted to the negative gradient of the given loss function  $L(y, F(x))$ .

$$F_m(x) = F_{m-1}(x) + \gamma_m h_m(x) \quad (14)$$

where  $F_m(x)$  is the model up to iteration  $m$ , and  $\gamma_m$  is the step size at iteration  $m$ .

- (4) Feedforward Neural Network (FFNN): FFNN is a feed-forward artificial neural network. It consists of at least three layers of nodes: an input layer, a hidden layer, and an output layer. Each node, except for the input nodes, is a neuron that uses a nonlinear activation function. The output  $y$  can be represented as:

$$y = f(W_2 f(W_1 x + b_1) + b_2) \quad (15)$$

where  $W_1$  and  $W_2$  are the weights,  $b_1$  and  $b_2$  are the biases, and  $f$  is the activation function. Besides, conventional deep learning has a strong impact on many applications because of its high capacity to learn the complex hidden representation of the data [73]. Therefore, we continue to explore two deep learning models as follows.

- (5) Convolution Neural Network (CNN): While CNN is more commonly used for image data, it can also be applied to sequential data. The convolutional layers capture local dependencies, and the fully connected layers predict the output. For a single convolutional layer followed by a fully connected layer, the output can be simplified as:

$$y = W_f \cdot (\text{flatten}(\text{ReLU}(W_c * x + b_c))) + b_f \quad (16)$$

where  $*$  denotes the convolution operation,  $W_c$  and  $b_c$  are the weights and biases of the convolutional layer,  $W_f$  and  $b_f$  are the weights and biases of the fully connected layer, and  $\text{ReLU}$  is the activation function.

- (6) Long Short-Term Memory (LSTM) [76,77]: LSTM is a type of recurrent neural network (RNN) that can learn order dependence in sequence prediction problems. For a single cell, the output  $h_t$  at time  $t$  is:

$$h_t = o_t \odot \tanh(c_t) \quad (17)$$

where  $o_t$  is the output gate,  $c_t$  is the cell state, and  $\odot$  denotes element-wise multiplication. The cell state is updated through a series of gates that control the flow of information:

$$f_t = \sigma(W_f \cdot [h_{t-1}, x_t] + b_f) \quad (18)$$

$$i_t = \sigma(W_i \cdot [h_{t-1}, x_t] + b_i) \quad (19)$$

$$\tilde{c}_t = \tanh(W_c \cdot [h_{t-1}, x_t] + b_c) \quad (20)$$

$$c_t = f_t \odot c_{t-1} + i_t \odot \tilde{c}_t \quad (21)$$

$$o_t = \sigma(W_o \cdot [h_{t-1}, x_t] + b_o) \quad (22)$$

Here,  $f_t$  is the forget gate,  $i_t$  is the input gate,  $\tilde{c}_t$  is the candidate cell state,  $\sigma$  is the sigmoid function, and  $W$  and  $b$  represent weights and biases for each gate, respectively.

### 2.2.2. Evaluation Metrics

Build a regression model, it's crucial to measure its performance using various evaluation metrics. These metrics help us understand how well the model has learned and predicted the outcomes. Below are the definitions and mathematical formulas for the metrics Mean Absolute Percentage Error (MAPE): MAPE is a measure of the prediction accuracy of a forecasting method in statistics. It expresses accuracy as a percentage of the error. It is calculated as:

$$\text{MAPE} = \frac{100\%}{n} \sum_{i=1}^n \left| \frac{y_i - y_{\text{pred},i}}{y_i} \right| \quad (23)$$

Mean Absolute Error (MAE): MAE is a measure of errors between paired observations expressing the same phenomenon. It's the average of the absolute errors between the predicted values and the actual values. It is calculated as:

$$\text{MAE} = \frac{1}{n} \sum_{i=1}^n |y_i - y_{\text{pred},i}| \quad (24)$$

RMSE is a quadratic scoring rule that also measures the average magnitude of the error. It's the square root of the average of squared differences between prediction and actual observation. It is calculated as:

$$\text{RMSE} = \sqrt{\frac{1}{n} \sum_{i=1}^n (y_i - y_{\text{pred},i})^2} \quad (25)$$

R-squared ( $R^2$ ), also known as the coefficient of determination, is a statistical measure of how close the data are to the fitted regression line. It is also known as the proportion of the variance in the dependent variable that is predictable from the independent variables. It is calculated as:

$$R^2 = 1 - \frac{\sum_{i=1}^n (y_i - y_{\text{pred},i})^2}{\sum_{i=1}^n (y_i - \bar{y})^2} \quad (26)$$

Where  $y_i$  is the true value,  $y_{\text{pred},i}$  is the predicted value,  $\bar{y}$  is the mean of the true values, and  $n$  is the number of observations.

## 3. Results and discussion

### 3.1. Results of MD Simulation

In this section, we investigate the effects of strain rates, temperatures, and grain sizes on the mechanical characteristics of AlCoCrCuFeNi HEA during tensile operations using molecular dynamic simulations. Fig. 2 shows the stress-strain relationship for AlCoCrCuFeNi HEA. The findings indicate that with rising temperatures, the stress in HEA samples initially decreases and then experiences a slight fluctuation around a tensile strain of approximately 0.05 before gradually stabilizing. Stress levels are also directly correlated with grain size and tensile speed. This is explained by the fact that in low-temperature samples, where most atoms oscillate close to their equilibrium positions, atoms' thermal mobility is comparatively restricted. High-temperature softening properties are observed as temperatures rise because of the atoms' higher kinetic energy, which decreases atomic interaction and atom-atom bond strength [78,79].

The phase change of the HEA specimen at different temperatures is depicted in Fig. 3, where the CNA method is used to color-code the atoms. All HEA specimens develop dislocations and stacking faults (SF) as a result of the elastic energy that has been stored being released during tension tests [80,81]. The phase change of the HEA sample under maximum stress is displayed in Fig. 3a. Fig. 3b shows a higher prevalence of the HCP structure of the polycrystal HEA specimen with a rise in strain value (0.2). The findings show that as simulation temperature rises, the number of unknown structures significantly increases. Simultaneously, the amorphous structure noticeably rises as the samples' HCP structure falls. This behavior can be explained by the fact that higher temperatures, as seen in Fig. 3b, enhance the kinetic energy of particles, magnifying thermal motion and increasing the amorphous appearance at grain borders. As a result, at grain boundaries, the proportion of amorphous structure increases with temperature.

As shown, Fig. 4 demonstrates that as strain ( $\epsilon$ ) increases, the composition of the face-centered cubic (FCC) structure decreases. In contrast, the body-centered cubic (BCC), hexagonal close-packed (HCP), and amorphous structures increase. This trend is particularly pronounced in the early stages of the pulling process, with a slight decrease in the FCC structure observed in the later stages. At higher temperatures, this trend becomes more apparent as the transformation into BCC, HCP, and amorphous structures, along with the disordered lattice during deformation, significantly increases the atomic ratio of the HCP and amorphous structure. This phenomenon is further explained in terms of the evolution structure of the atomic of AlCoCrCuFeNi HEA in Fig. 3.

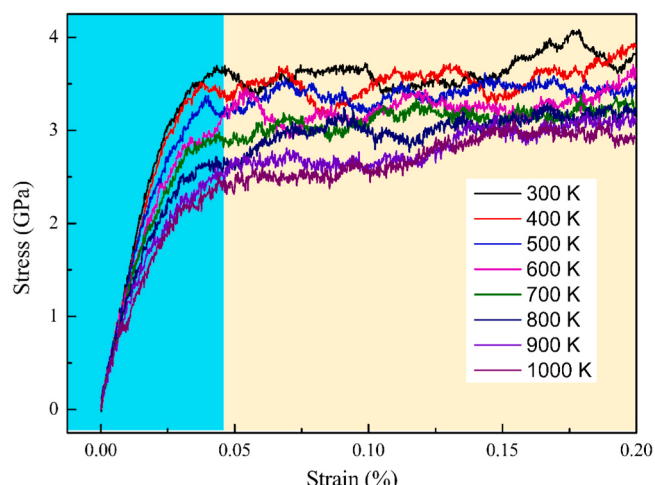


**Fig. 2.** The stress-strain of tensile for polycrystalline AlCoCrCuFeNi HEA with various temperatures.

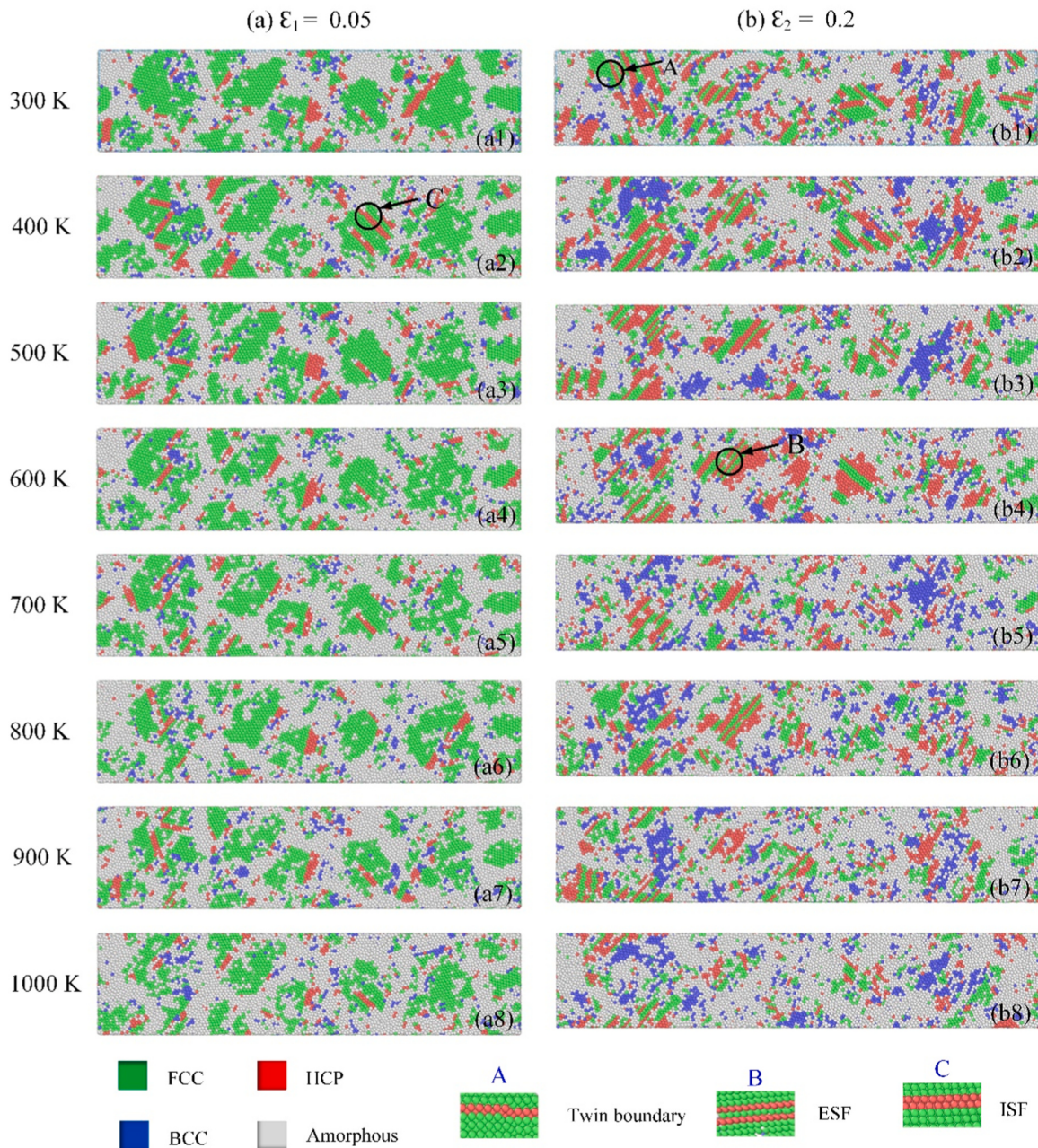


**Fig. 3.** The CNA of polycrystalline of AlCoCrCuFeNi HEA with different strain values under various temperatures.

**Fig. 5** displays the dislocation distribution in HEA workpieces, as identified through DXA analysis with various temperatures during tension simulation. The degree of dislocation movement determines how flexible metal materials are [82,83]. Meanwhile, the ability to move in dislocations affects the strength of HEA samples. **Fig. 5a** shows the dislocation distribution in the HEA sample at ultimate stress. Because of the impacts of workpiece production and annealing processes on the occurrence of GB dislocations in the manufactured HEA samples, dislocations are initially concentrated mostly at the GB. As the temperature rises, **Fig. 4b** shows that all specimens with a strain value of 0.2 exhibit a large number of Shockley partial dislocations, though their frequency decreases. This implies that, with more robust dislocation nucleation at lower temperatures, lower temperatures increase the efficacy of slip behavior generated by Shockley partial dislocations. Because dislocation emission and nucleation at lower temperatures demand a greater external force, the average flow stress and ultimate strength at lower

temperatures are greater than those at higher temperatures. The results show that high temperatures hinder the emission and propagation of dislocations. Amorphization inhibits the sliding activation system, as **Fig. 5b** shows, and this impact becomes more noticeable at higher temperatures. This finding emphasizes how the amorphous structural barrier becomes more prominent as temperature rises [84], which lowers dislocation at higher temperatures.

Finally, we have the statistical analysis in **Table 1** summarize the properties of a dataset encompassing 22,021 observations across five parameters: strain, temperature, grain size, strain rate, and output. The strain has a fairly uniform distribution with a mean close to the median, ranging from 0 to 0.2. The temperature shows a wide spread, averaging 427.28 K, but with half the values at the minimum of 300 K, suggesting a lower-bound skew. Grain size exhibits less variability, with most data points clustered around the mean of 29.1 and the majority at 20 grain. The strain rate reveals a vast range and high variability, with an average

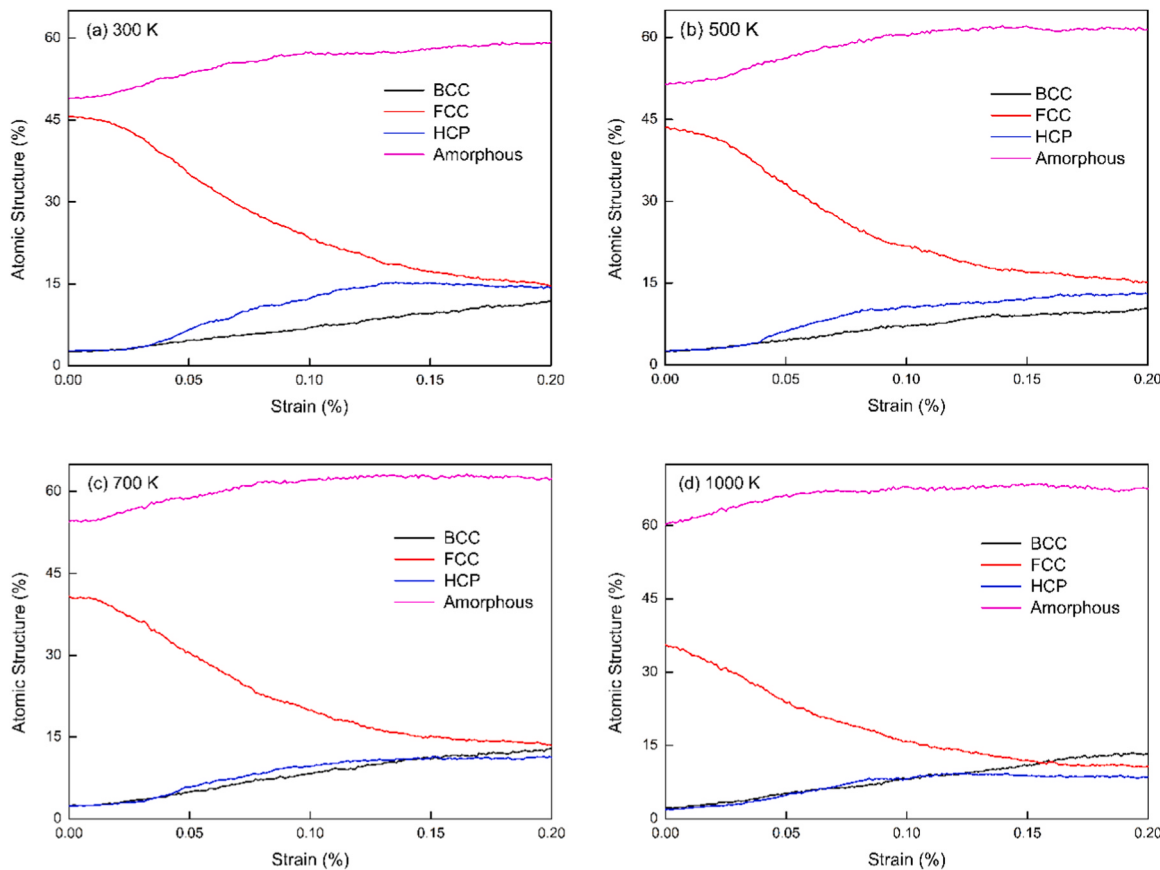


**Fig. 4.** Evolutions structure of atomic percentages of HEA with various temperatures under tension process.

of  $2.4 \times 10^9$  s<sup>-1</sup>, suggesting potential outliers or a heavy-tailed distribution. Lastly, the output has an average of 3.35 and a moderately widespread, with values from -0.017–5.75. The quartile data for both temperature and grain size indicate a significant number of observations at their lower limits, while the strain rate's large standard deviation points to a diverse range of values. Collectively, these statistics suggest the data exhibits a mix of uniform and skewed distributions, with certain parameters showing potential boundary effects or outliers

### 3.2. Results of Machine Learning Algorithms Prediction

In this study, setup was executed on the powerful GPUs provided by OpenSource Google Colab's cloud service. We utilized the scikit-learn library and the Keras framework within a Python environment to implement our models. The data for each experiment was divided into two sets: 70 % for training purposes and 30 % for evaluation to assess the model's performance.

Drawing insights from prior research on optimizing neural network structures, we adopted strategies to improve our model's performance and ensure its stability. This included the integration of dropout techniques, with a set probability of 0.25, to prevent overfitting by randomly omitting units during training. Additionally, we chose the GlorotNormal kernel initializer for its efficacy in maintaining a unit's output variance proportional to its input variance, thereby optimizing the initialization of the network's weights. We also implemented batch normalization to accelerate training and enhance performance by normalizing each layer's inputs. These hyper-parameters were carefully chosen and fine-tuned to achieve the best possible model performance.

Table 2 provides a detailed comparison of hyperparameters used in three different deep learning models: FFNN, CNN, and LSTM. For the FFNN model, there are 3 hidden layers, 400 neurons per layer, a batch size of 32, a dropout rate of 0.25, a learning rate of  $6 \times 10^{-4}$ , and it uses

the Adam optimizer with a total of 323,201 parameters, amounting to 1.23 MB. The CNN model is configured with 4 hidden layers, 356 neurons, a consistent batch size of 32, a dropout rate of 0.25, a lower learning rate of  $1 \times 10^{-4}$ , also utilizes the Adam optimizer, and has 128,161 parameters, totaling 500.63 KB. Lastly, the LSTM model mirrors the FFNN in terms of hidden layers and neurons, sharing the same batch size, dropout rate, and optimizer, but has a learning rate of  $1 \times 10^{-4}$  and significantly more parameters, totaling 3206801, which is approximately 12.23 MB. This summary highlights the distinctive configurations and scales of these models, showcasing their varied approaches to handling neural network tasks.

In the presented Table 3, the performance of various machine learning models is evaluated across four metrics, with the LSTM model demonstrating superior results in each category. It boasts the lowest Mean Absolute Percentage Error (MAPE) at 16.21, indicating the smallest average prediction error in percentage terms compared to other models. The LSTM also leads in Mean Absolute Error (MAE) with a value of 0.072, suggesting its predictions are the closest to the true values. Furthermore, with the lowest RMSE of 0.095, the LSTM model's predictions are shown to have the smallest variance from the actual data. Lastly, an R-squared ( $R^2$ ) value of 0.99 for the LSTM model means it explains 99 % of the variance in the dataset, which is the highest among the models compared, indicating an exceptionally good fit to the data. These results collectively highlight the LSTM's robust predictive ability, outperforming other models such as Linear Regression, Support Vector Regression, Gradient Boosting Regressor, Feedforward Neural Network, and Convolutional Neural Network across the board in this specific experiment.

The provided Fig. 7 illustrates the loss of an LSTM model throughout 50 epochs of training. Initially, both the training and validation loss decrease sharply, indicating significant learning from the model in the early stages. As the epochs progress, the loss for both datasets levels off,

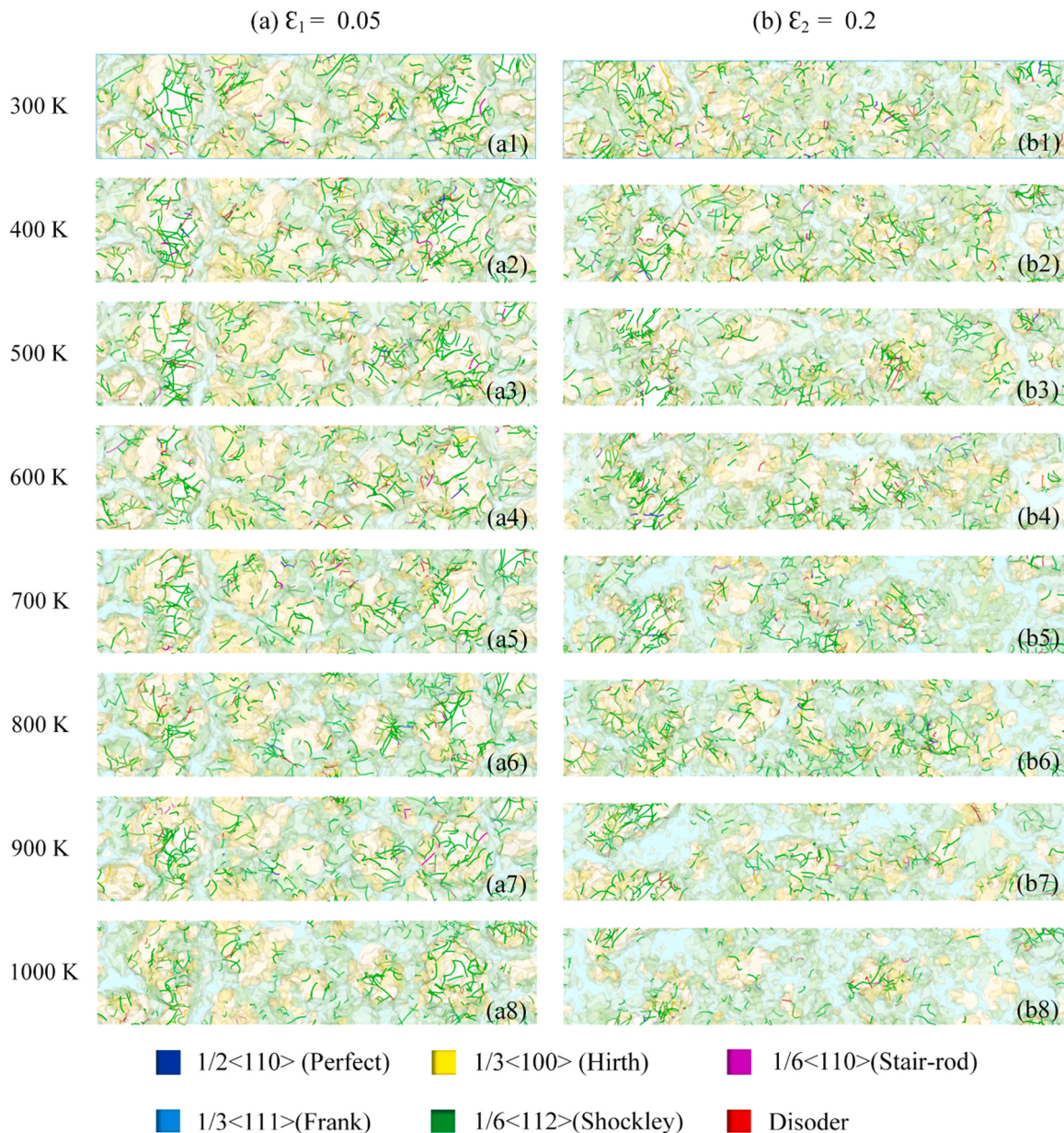
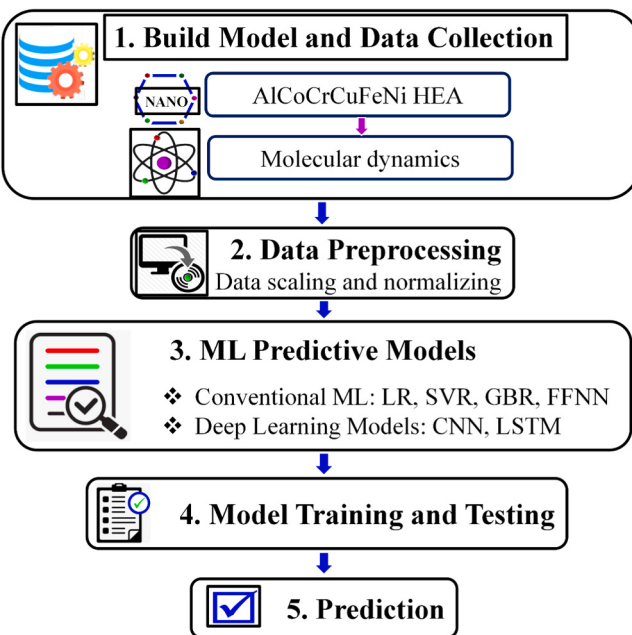


Fig. 5. The dislocation distribution of polycrystalline of AlCoCrCuFeNi HEA samples with different strain values and various temperatures.

suggesting that the model is converging to an optimal state and that further training yields minimal improvement. Notably, the training and validation loss values remain closely aligned, which is indicative of a well-generalized model that is not overfitting to the training data. The graph also demonstrates a stable and smooth reduction in loss, likely due to a well-chosen learning rate and batch size. The low final loss values for both training and validation suggest that the LSTM has achieved a strong predictive performance on the dataset. However, while the graph indicates a successful training process, additional metrics would be necessary to fully evaluate the model's performance across different aspects, such as accuracy and recall, and it would be prudent to further assess the model using a separate test dataset to ensure its efficacy in real-world applications.

Fig. 8 shows two bar charts comparing feature importance from a machine learning model, specifically focusing on multicollinear features within a training dataset. On the left, we have a bar chart titled "Impurity-based vs. permutation importance on multicollinear features (train set)." This chart displays the Gini importance of four features: "Strain," "Temperature," "Strain rate," and "Grain size." The Gini

importance is a metric used in decision trees and tree ensemble methods like Random Forest to estimate the importance of a feature by measuring how much the tree nodes that use that feature reduce impurity on average (e.g., Gini impurity or entropy). In this chart, "Strain" has the highest Gini importance, followed by "Temperature" and "Strain rate", with "Grain size" having the least importance. On the right side of the image, there is another bar chart with error bars representing the permutation importance of the same features. Permutation importance is calculated by observing how each predictor feature's random reordering (permutation) affects the model performance. The chart shows "Decrease in accuracy score" on the x-axis, which indicates the impact on the model's accuracy when the values of each feature are shuffled. The "Strain" feature has the largest decrease in accuracy, which suggests it has the highest importance based on this method. The error bars indicate the variability or confidence interval of this important measure. Overall, the image suggests an experiment where the importance of features in a predictive model is assessed by two different methods: Gini importance and permutation importance. The experiment likely aims to investigate how multicollinearity (a situation where two or more



**Fig. 6.** Schematic Workflow of the ML predictive model for stress values.

**Table 2**  
Detail hyper-parameters summarization for the implementation.

	Models		
Hyperparameters	FFNN	CNN	LSTM
Hidden layers	3	4	3
Number of neurons	400	356	400
Batch size	32	32	32
Dropout	0.25	0.25	0.25
Learning rate	$1.0 \times 10^{-4}$	$1.0 \times 10^{-4}$	$1.0 \times 10^{-4}$
Optimizer	Adam	Adam	Adam
Total parameters	323201 (1.23 MB)	128161 (500.63 KB)	3206801 (12.23 MB)

**Table 3**  
Performance comparison for machine learning predictive models.

Evaluation	LR	SVR	GBR	FFNN	CNN	LSTM
MAPE	318.17	136.13	468.9	21.32	193.06	16.21
MAE	0.422	0.202	0.91	0.092	0.178	0.072
RMSE	0.615	0.298	1.25	0.12	0.267	0.095
R <sup>2</sup>	0.100	0.85	0.98	0.98	0.90	0.99

features are highly correlated) affects these important measures. Notably, “Strain” seems to be the most significant predictor in both methods, while “Grain size” is the least important.

Fig. 9 shows the permutation importance of features on a test dataset, presumably following the same methodology as the training set described previously. Permutation importance is calculated by randomly shuffling a feature in the test dataset and determining the change in the model’s accuracy. In this chart, we see the following features listed from top to bottom: “Strain”, “Strain rate”, “Temperature”, and “Grain

size”. Similar to the previous image for the training set, the x-axis represents the “Decrease in accuracy score”, indicating the impact on the model’s accuracy when the values of each feature are shuffled. The feature “Strain” has multiple points plotted with error bars, suggesting that the permutation importance was calculated several times, perhaps through a cross-validation process or different test sets, to estimate variability or confidence intervals. The points for “Strain” are scattered with a wide range of values but generally indicate a high decrease in

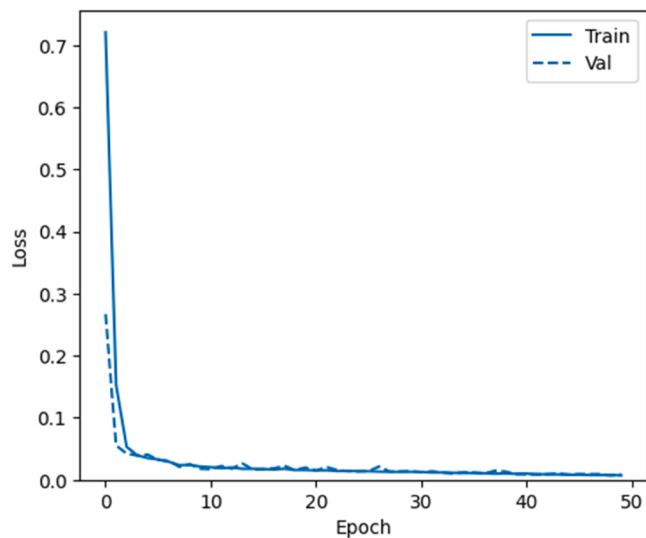


**Fig. 7.** LSTM Learning curve during training (train) and validation (val).

accuracy when this feature is permuted, meaning it is likely an important feature. “Strain rate” and “Temperature” have less variability and show a moderate decrease in accuracy, which points to their lesser but still significant importance. “Grain size” shows the smallest decrease in accuracy, suggesting it has the least importance according to this method on the test set. The spread of the points for “Strain” could indicate that the test sets have varying characteristics or that the feature’s importance is highly sensitive to the data it is tested on, a common situation when dealing with multicollinear features. The error bars for each feature give an indication of the reliability of these importance measures; wider bars suggest greater variability in the importance estimate across different test scenarios. Overall, the chart is used to assess the stability of the feature importance across different subsets of data, providing insights into how model performance might generalize to unseen data.

As illustrated in Fig. 10, the model’s predictions align closely with actual values, as evidenced by an R-squared value of 0.99, a Mean Absolute Error (MAE) of 0.072, a RMSE of 0.095, and a Mean Absolute Percentage Error (MAPE) of 16.21, signaling robust predictive capabilities. Furthermore, the figure illustrates that the LSTM model’s stress value predictions invariably match the range of actual values. This accuracy extends over 6000 data points, affirming the model’s consistent validation. Compared to alternative models, the LSTM model distinctly outperforms them, showcasing superior precision and lower error margins.

As illustrated in Fig. 11 provided appears to be a scatter plot comparing predicted values from an LSTM model against actual values. The X-axis is labeled “Actual values,” and the Y-axis is labeled “Predicted values,” suggesting that each point on the graph represents a pair of actual and predicted values for a certain data point. The data points are plotted as red crosses, and there seems to be a blue line that may indicate the ideal situation where the predicted values perfectly match the actual values (a 45-degree line where predicted equals actual). The concentration of red crosses around this blue line indicates that the LSTM model predictions closely align with the actual values. The closer these points are to the blue line, the more accurate the predictions are. The title “Nano strain” could imply that the model is predicting some form of strain at the nanoscale, which could be relevant in fields such as materials science or structural engineering. Overall, the scatter plot suggests that the LSTM model has a good performance, with the majority of predictions falling near the ideal line. However, a more detailed analysis cannot be provided without more context, such as the range of values, units, or specific applications.

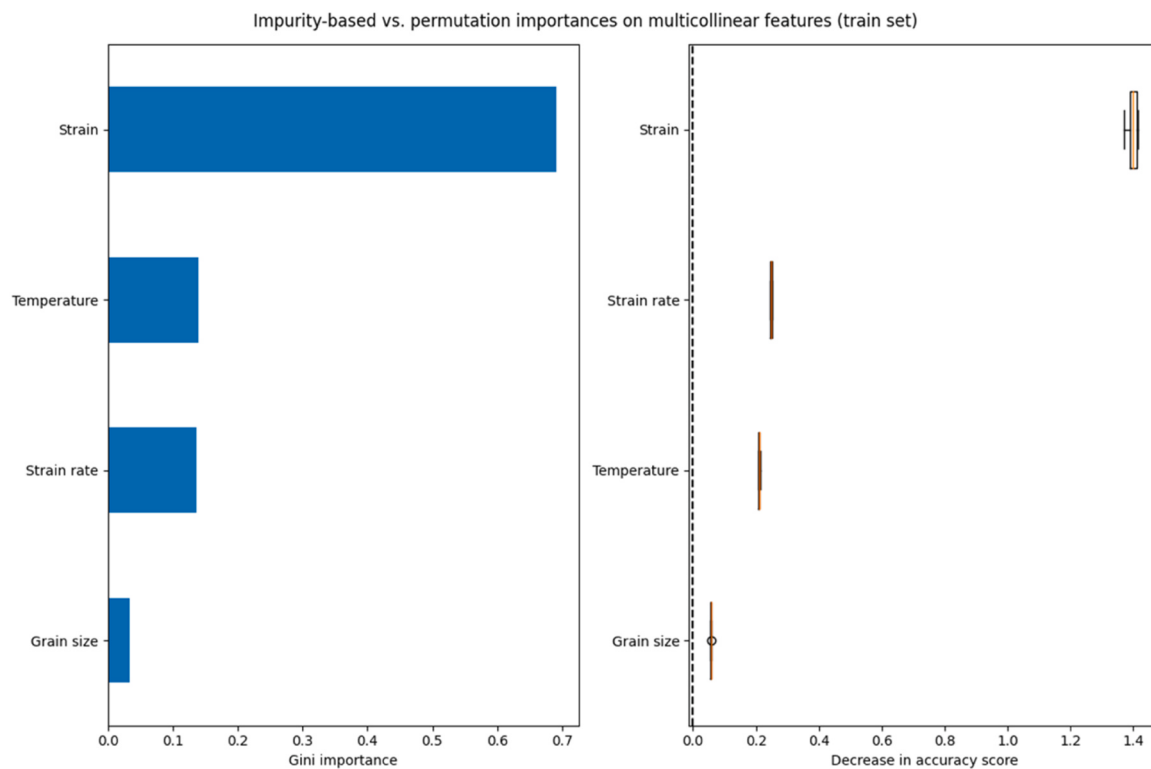


**Fig. 8.** Feature importance regarding tensile deformation during training.

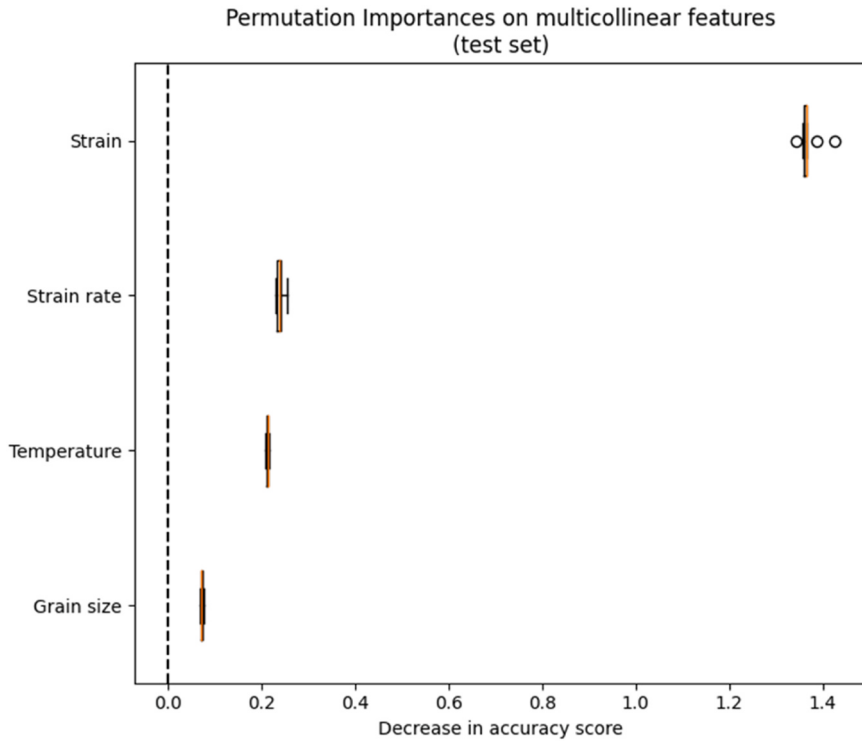


**Fig. 9.** Feature importance regarding tensile deformation during validation.

Studies on these alloy systems have revealed diverse mechanical properties during tensile testing, influenced by factors such as temperature, grain size, and tensile speed. The study delves into a comprehensive understanding of high-entropy alloys. Notably, this research distinguishes itself by integrating tensile deformation into models,

utilizing a combination of molecular dynamics simulation and machine learning, setting it apart from previous studies. The tensile strength aligns closely with Afkham et al. [20] findings, and while the temperature and strain rate exceed Elgack et al. [21] results, they are in line with Wang et al. [29] experimental observations. A comparison of

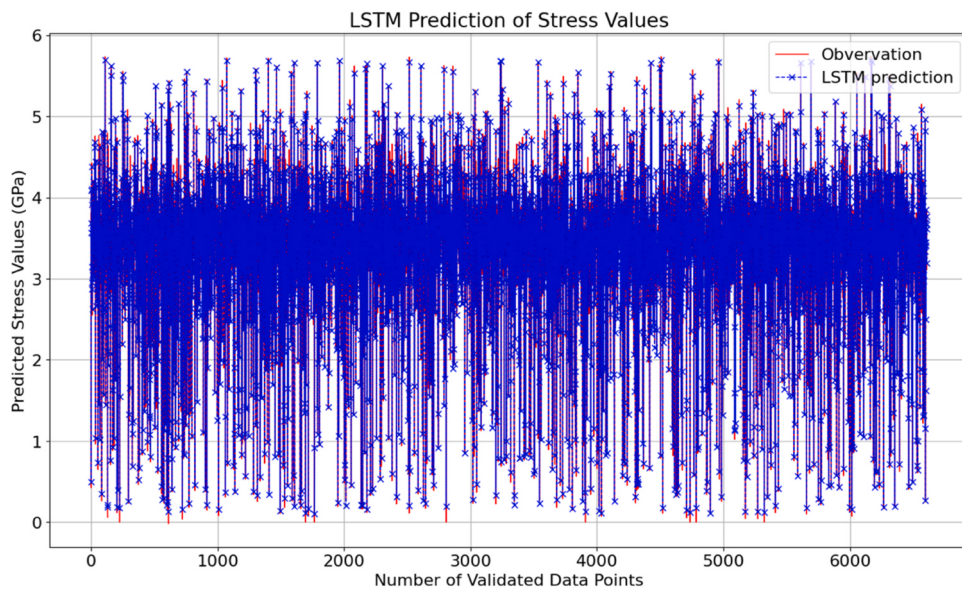


**Fig. 10.** Highlights the LSTM model's exceptional predictive accuracy within training and testing datasets.

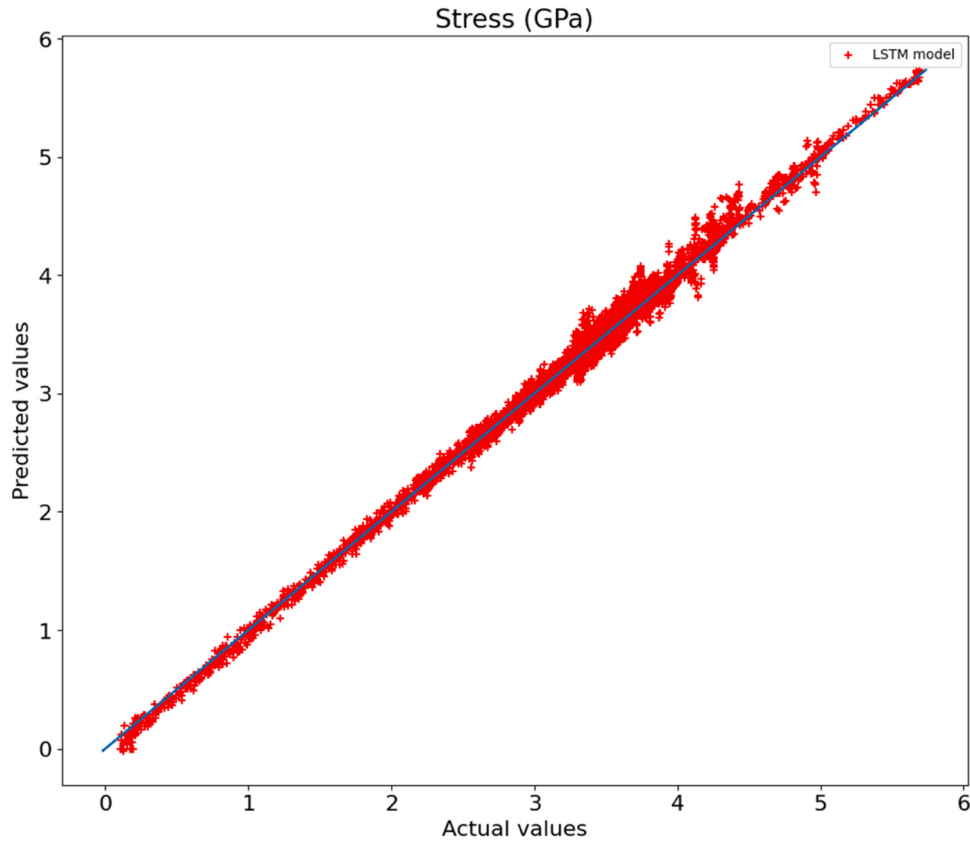


**Fig. 11.** The prediction precision of LSTM compared to actual observation.

mechanical properties across various reports is presented in [Table 4](#), supports the study's conclusions, reinforcing consistency with previous research. The hope is that these findings will prove informative and valuable for future investigations into AlCoCrCuFeNi HEA.

#### 4. Conclusions

MD simulations and machine learning are used to examine how the

mechanical characteristics and deformation behavior of AlCoCrCuFeNi HEA samples are affected by temperature, tension strain rate, and grain size.

The AlCoCrCuFeNi HEA sample softens at high temperatures, which lowers the interatomic linking force. Young's modulus, average flow stress, and ultimate stress are all decreased as a result. In addition, the expansion of the amorphization zone caused by the temperature increase results in a reduction of the total dislocation length. Additionally,

**Table 4**

The comparison of several results between this study and other research.

Materials	Strain rate (s <sup>-1</sup> )	Temperature (K)	Strain (%)	Stress (GPa)	Method	Reference
This study	$10^8 - 2 \times 10^{10}$	300–1000	20	3.12–5.75	MD and ML	
Al <sub>x</sub> CoCrCuFeNi	$10^{10}$	700–2200	40	-	MD	Bahramyan et al. [15]
Fe <sub>50</sub> Mn <sub>30</sub> Co <sub>10</sub> Cr <sub>10</sub>	$6 \times 10^{-3}$	RT	0.46–1.2	0.8	Experimental	Niendorf et al. [18]
AlCrCoFeCuNi	$10^9 - 10^{11}$	300–1300	40	0.6–5.5	MD	Afkham et al. [20]
FeNiCrCoCu	-	200–400	-	0.1367–2.158	MD and ML	Elgack et al. [21]
AlCoCrCuFeNi	$1 \times 10^{-3}$	300–1473	27	1.482–1.795	Experimental	Deng et al. [23]
Al <sub>2</sub> CoCrFeNi	-	1273–1573	-	1.21–1.3	Experimental	Shi et al. [27]
CoCrCuFeNiAl <sub>0.5</sub>	$10^{-4} - 8 \times 10^{-4}$	RT	50	0.707–24.5	Experimental	Wang et al. [28]
Al	$1.7 \times 10^8$	300	-	2.1–4.2	MD and ML	Mayer et al. [44]

\*RT: Room Temperature

we have implemented different ML algorithms for the predictive model. Experimentally, the results indicate that the LSTM model outperforms all other models in each of the metrics. Specifically, the LSTM achieved the lowest MAPE (16.21), which signifies that it has the smallest average percentage deviation from the actual values, making it highly accurate in percentage error. Additionally, the LSTM model recorded the lowest MAE (0.072) and RMSE (0.095), indicating that, on average, its predictions are the closest to the actual values and it has the smallest spread of errors, respectively. Furthermore, the LSTM model achieved the highest R<sup>2</sup> score (0.99), which suggests that it is able to explain 99 % of the variance in the target variable, indicating an exceptional level of predictive power and model fit.

Our study demonstrates that machine learning models, particularly the LSTM, provide a robust framework for evaluating interatomic potentials with high accuracy in predicting tensile strength and deformation behavior, as well as capturing the effects of strain and temperature. To maximize the utility of such analyses, we recommend selecting models that demonstrate superior performance across multiple metrics, implementing cross-validation and robustness testing, and integrating feature importance analysis to guide experimental efforts. Additionally, combining these predictive models with molecular dynamics simulations and benchmarking against experimental data can further refine the accuracy of interatomic potentials. However, our findings also highlight areas where the models are less accurate, such as the effects of grain size and the presence of multicollinearity among features like strain, strain rate, and temperature. Addressing these inaccuracies will require gathering more granular data and exploring advanced techniques for feature selection and model tuning. By focusing on these areas, future research can enhance the predictive power and reliability of interatomic potentials in material science.

In conclusion, the LSTM model not only shows the best performance in each individual metric but does so with a significant margin over other models like Linear Regression, Support Vector Regression, Gradient Boosting Regression, Feedforward Neural Network, and Convolutional Neural Network. The superiority of the LSTM model in this comparison suggests that its ability to capture temporal dynamics in the data is particularly effective for the predictive task at hand, making it the preferred choice among the evaluated models.

#### CRediT authorship contribution statement

**Hoang-Giang Nguyen:** Writing – review & editing, Writing – original draft, Visualization, Validation, Software, Investigation, Formal analysis, Data curation, Conceptualization. **Thanh-Dung Le:** Writing – review & editing, Software, Formal analysis, Data curation, Conceptualization. **Hong-Giang Nguyen:** Writing – review & editing, Validation, Software, Formal analysis. **Te-Hua Fang:** Supervision, Resources, Project administration, Methodology, Data curation.

#### Declaration of Competing Interest

The authors declare the following financial interests/personal relationships which may be considered as potential competing interests: Te-Hua Fang reports financial support and administrative support were provided by National Kaohsiung University of Science and Technology. Te-Hua Fang reports a relationship with National Kaohsiung University of Science and Technology that includes: funding grants. Te-Hua Fang reports a relationship with Te-Hua Fang that includes: funding grants. Te-Hua Fang has patent pending to NSTC 113-2221-E-992-067-MY3 and Industry Cooperation Project no. 113A00262. Hoang-Giang Nguyen<sup>1,4</sup>, Thanh-Dung Le<sup>2</sup>, Hong-Giang Nguyen<sup>3</sup>, Te-Hua Fang<sup>1,5</sup>,

\* <sup>1</sup>Department of Mechanical Engineering, National Kaohsiung University of Science and Technology, Kaohsiung 807, Taiwan <sup>2</sup>Department of Electrical Engineering, École de Technologie Supérieure, University of Québec, Montréal, Québec, Canada <sup>3</sup>Institute of Testing and Quality Assurance in Education, Hue University, Hue City 49000, Viet Nam <sup>4</sup>Faculty of Engineering and Technology, Kien Giang University, Kien Giang Province, Viet Nam <sup>5</sup>Department of Fragrance and Cosmetic Science, Kaohsiung Medical University, Kaohsiung 807, Taiwan. If there are other authors, they declare that they have no known competing financial interests or personal relationships that could have appeared to influence the work reported in this paper.

#### Data Availability

The authors do not have permission to share data.

#### Acknowledgments

The authors acknowledge the support by the National Science and Technology Council, Taiwan, under grant number NSTC 113-2221-E-992-067-MY3 and Industry Cooperation Project no. 113A00262.

#### References

- [1] C. Cazorla, J. Boronat, Simulation and understanding of atomic and molecular quantum crystals, *Rev. Mod. Phys.* **89** (3) (2017) 035003.
- [2] B. Leimkuhler, C. Matthews, Molecular dynamics, *Interdiscip. Appl. Math.* **39** (2015) 443.
- [3] F. Paesani, Getting the right answers for the right reasons: Toward predictive molecular simulations of water with many-body potential energy functions, *Acc. Chem. Res.* **49** (9) (2016) 1844–1851.
- [4] Z. Hashemi, O. Abouali, G. Ahmadi, Direct numerical simulation of particle-fluid interactions: a review, *Iran. J. Sci. Technol., Trans. Mech. Eng.* **41** (2017) 71–89.
- [5] A. Carmona-Orbezo, R.A. Dryfe, Understanding the performance of flow-electrodes for capacitive deionization through hydrodynamic voltammetry, *Chem. Eng. J.* **406** (2021) 126826.
- [6] G.F. Bomarito, Y. Lin, D.H. Warner, An atomistic modeling survey of the shear strength of twist grain boundaries in aluminum, *Scr. Mater.* **101** (2015) 72–75.
- [7] V.S. Krasnikov, A.E. Mayer, Dislocation dynamics in aluminum containing Α' phase: Atomistic simulation and continuum modeling, *Int. J. Plast.* **119** (2019) 21–42.
- [8] J. Kacher, B.P. Eftink, B. Cui, I.M. Robertson, Dislocation interactions with grain boundaries, *Curr. Opin. Solid State Mater. Sci.* **18** (4) (2014) 227–243.
- [9] J. Davoodi, S. Dadashi, M. Yarifard, Molecular dynamics simulations of the melting of Al-Ni nanowires, *Philos. Mag.* **96** (22) (2016) 2300–2310.

- [10] M. Bahramyan, R.T. Mousavian, D. Brabazon, Molecular dynamic simulation of edge dislocation-void interaction in pure Al and Al-Mg alloy, *Mater. Sci. Eng.: A* **674** (2016) 82–90.
- [11] H.G. Nguyen, M.J. Wu, T.H. Fang, Study on copper-to-copper bonding of three-dimensional integrated circuits using the quasicontinuum method, *Phys. Scr.* **99** (6) (2024) 065114.
- [12] Y. Zhang, T.T. Zuo, Z. Tang, M.C. Gao, K.A. Dahmen, P.K. Liaw, Z.P. Lu, Microstructures and properties of high-entropy alloys, *Prog. Mater. Sci.* **61** (2014) 1–93.
- [13] S. Zhao, G.M. Stocks, Y. Zhang, Stacking fault energies of face-centered cubic concentrated solid solution alloys, *Acta Mater.* **134** (2017) 334–345.
- [14] H.G. Nguyen, T.H. Fang, D.Q. Doan, Cyclic plasticity and deformation mechanism of AlCrCuFeNi high entropy alloy, *J. Alloy. Compd.* **940** (2023) 168838.
- [15] M. Bahramyan, R.T. Mousavian, D. Brabazon, Determination of atomic-scale structure and compressive behavior of solidified AlxCrCoFeCuNi high entropy alloys, *Int. J. Mech. Sci.* **171** (2020) 105389.
- [16] R.S. Ganji, P.S. Karthik, K.B.S. Rao, K.V. Rajulapati, Strengthening mechanisms in equiatomic ultrafine grained AlCoCrCuFeNi high-entropy alloy studied by micro- and nanoindentation methods, *Acta Mater.* **125** (2017) 58–68.
- [17] H.G. Nguyen, T.H. Fang, Machining mechanism and residual stress of AlCuCrFeNi alloy, *Int. J. Mech. Sci.* (2024) 109429.
- [18] T. Niendorf, T. Wegener, Z. Li, D. Raabe, Unexpected cyclic stress-strain response of dual-phase high-entropy alloys induced by partial reversibility of deformation, *Scr. Mater.* **143** (2018) 63–67.
- [19] E.J. Pickering, H.J. Stone, N.G. Jones, Fine-scale precipitation in the high-entropy alloy Al0.5CrFeCoNiCu, *Mater. Sci. Eng.: A* **645** (65–71) (2015).
- [20] Y. Afkham, M. Bahramyan, R.T. Mousavian, D.J.M.S. Brabazon, Tensile properties of AlCrCoFeCuNi glassy alloys: A molecular dynamics simulation study, *Mater. Sci. Eng.: A* **698** (2017) 143–151.
- [21] O. Elgack, B. Almomani, J. Syarif, M. Elzab, M. Irshaid, M. Al-Shabi, Molecular dynamics simulation and machine learning-based analysis for predicting tensile properties of high-entropy FeNiCrCoCu alloys, *J. Mater. Res. Technol.* **25** (2023) 5575–5585.
- [22] Y. Wang, R. Li, P. Niu, Z. Zhang, T. Yuan, J. Yuan, K. Li, Microstructures and properties of equimolar AlCoCrCuFeNi high-entropy alloy additively manufactured by selective laser melting, *Intermetallics* **120** (2020) 106746.
- [23] N. Deng, J. Wang, J. Wang, Y. He, E. Beaugnon, J. Li, Effect of high magnetic field assisted heat treatment on microstructure and properties of AlCoCrCuFeNi high-entropy alloy, *Mater. Lett.* **303** (2021) 130540.
- [24] Y.J. Zhao, J.W. Qiao, S.G. Ma, M.C. Gao, H.J. Yang, M.W. Chen, Y. Zhang, A hexagonal close-packed high-entropy alloy: The effect of entropy, *Mater. Des.* **96** (2016) 10–15.
- [25] L. Xie, P. Brault, A.L. Thomann, X. Yang, Y. Zhang, G. Shang, Molecular dynamics simulation of Al–Co–Cr–Cu–Fe–Ni high entropy alloy thin film growth, *Intermetallics* **68** (2016) 78–86.
- [26] Y. Gao, H.M. Urbasen, Scratching of nanocrystalline metals: A molecular dynamics study of Fe, *Appl. Surf. Sci.* **389** (2016) 688–695.
- [27] Y. Shi, Q. Shu, P.K. Liaw, M. Wang, C.L. Teng, H. Zou, J. Wang, Effect of annealing on mechanical and thermoelectric properties of a Al2CoCrFeNi high-entropy alloy, *Mater. Des.* **213** (2022) 110313.
- [28] F. Wang, Y. Zhang, G. Chen, H.A. Davies, Tensile and compressive mechanical behavior of a CoCrCuFeNiAl 0.5 high entropy alloy, *Int. J. Mod. Phys. B* **23** (06n07) (2009) 1254–1259.
- [29] Z. Wang, Q. Fang, J. Li, B. Liu, Y. Liu, Effect of lattice distortion on solid solution strengthening of BCC high-entropy alloys, *J. Mater. Sci. Technol.* **34** (2) (2018) 349–354.
- [30] X.D. Xu, P. Liu, S. Guo, A. Hirata, T. Fujita, T.G. Nieh, M.W. Chen, Nanoscale phase separation in a fcc-based CoCrCuFeNiAl0.5 high-entropy alloy, *Acta Mater.* **84** (2015) 145–152.
- [31] Y.K. Kim, J. Choe, K.A. Lee, Selective laser melted equiatomic CoCrFeMnNi high-entropy alloy: Microstructure, anisotropic mechanical response, and multiple strengthening mechanism, *J. Alloy. Compd.* **805** (2019) 680–691.
- [32] H.G. Nguyen, T.H. Fang, Mechanics of AlCuNiTi alloy orthogonal micro-cutting, *Model. Simul. Mater. Sci. Eng.* **31** (8) (2023) 085016.
- [33] N. Haghjadian, S. Primit, M. Annasamy, P. Cizek, P.D. Hodgson, D.M. Fabijanic, On the hot-worked microstructure of face-centered cubic Al0.3CoCrFeNi high entropy alloy, *Scr. Mater.* **178** (2020) 144–149.
- [34] Q. Fang, M. Yi, J. Li, B. Liu, Z. Huang, Deformation behaviors of Cu29Zr32Ti15Al5Ni19 high entropy bulk metallic glass during nanoindentation, *Appl. Surf. Sci.* **443** (2018) 122–130.
- [35] Y.X. Li, Q.K. Raymond Kwesi Nutor, X.P. Zhao, Q.P. Zhang, S.S. Cao, X.D. Sohn, Wang, et al., Unraveling the deformation behavior of the Fe45Co25Ni10V20 high entropy alloy, *Int. J. Plast.* **165** (2023) 103619.
- [36] N. Wang, R.K. Nutor, Y.X. Li, Q.P. Cao, S.Q. Ding, X.D. Wang, J.Z. Jiang, Tuning mechanical properties of high entropy alloys by electro-pulsing method, *J. Alloy. Compd.* **902** (2022) 163684.
- [37] Y. Li, Y. Chen, R.K. Nutor, N. Wang, Q. Cao, X. Wang, J.Z. Jiang, Plasticity Improvement in a Co-Rich Co40Fe25Cr20Ni15 High-Entropy Alloy via Al Alloying, *Materials* **16** (3) (2023) 1149.
- [38] A.M. Manzoni, S. Singh, H.M. Daoud, R. Popp, R. Völkli, U. Glatzel, N. Wanderka, On the path to optimizing the Al-Co-Cr-Cu-Fe-Ni-Ti high entropy alloy family for high temperature applications, *Entropy* **18** (4) (2016) 104.
- [39] L. Lu, J. Li, C.Y. Su, P.Y. Sun, L. Chang, B.B. Zhou, C.Y. Zhou, Research on fatigue crack growth behavior of commercial pure titanium base metal and weldment at different temperatures, *Theor. Appl. Fract. Mech.* **100** (2019) 215–224.
- [40] D.H. Chen, X.L. Fan, Evaluation of the brittle failure of blunt U-shaped notch under mode I loading, *Eng. Fract. Mech.* **214** (2019) 40–61.
- [41] A.T. AlMotaseem, J. Bergström, A. Gåård, P. Krakhmalev, L.J. Holleboom, Tool microstructure impact on the wear behavior of ferrite iron during nanoscratching: An atomic level simulation, *Wear* **370** (2017) 39–45.
- [42] C.H. Wang, K.C. Chao, T.H. Fang, I. Stachiv, S.F. Hsieh, Investigations of the mechanical properties of nanoimprinted amorphous Ni–Zr alloys utilizing the molecular dynamics simulation, *J. Alloy. Compd.* **659** (2016) 224–231.
- [43] J.A. Keith, V. Vassilev-Galindo, B. Cheng, S. Chmiela, M. Gastegger, K.R. Müller, A. Tkatchenko, Combining machine learning and computational chemistry for predictive insights into chemical systems, *Chem. Rev.* **121** (16) (2021) 9816–9872.
- [44] A.E. Mayer, V.S. Krasnikov, V.V. Pogorelko, Dislocation nucleation in Al single crystal at shear parallel to (111) plane: Molecular dynamics simulations and nucleation theory with artificial neural networks, *Int. J. Plast.* **139** (2021) 102953.
- [45] Y. Zhang, Y. Yue, Simulation and Calculation for Predicting Structures and Properties of High-Entropy Alloys, IntechOpen, 2023, <https://doi.org/10.5772/intechopen.105963>.
- [46] J. Chen, P. Niu, Y. Liu, Y. Lu, X. Wang, Y. Peng, J. Liu, Effect of Zr content on microstructure and mechanical properties of AlCoCrFeNi high entropy alloy, *Mater. Des.* **94** (2016) 39–44.
- [47] H.G. Nguyen, T.H. Fang, Plastic deformation in nanoindentation of Alx(CuCrFeNi)1-x high entropy alloy, *J. Alloy. Compd.* **968** (2023) 172172.
- [48] A. Sharma, S.A. Deshmukh, P.K. Liaw, G. Balasubramanian, Crystallization kinetics in AlCrCoFeNi (0 ≤ x ≤ 40) high-entropy alloys, *Scr. Mater.* **141** (2017) 54–57.
- [49] N. Grönbech-Jensen, Complete set of stochastic Verlet-type thermostats for correct Langevin simulations, *Mol. Phys.* **118** (8) (2020) e1662506.
- [50] N. Grönbech-Jensen, O. Farago, Defining velocities for accurate kinetic statistics in the Grönbech-Jensen Farago thermostat, *Phys. Rev. E* **101** (2) (2020) 022123.
- [51] M. Purse, G. Edmund, S. Hall, B. Howlin, I. Hamerton, S. Till, Reactive molecular dynamics study of the thermal decomposition of phenolic resins, *J. Compos. Sci.* **3** (2) (2019) 32.
- [52] P.K. Patra, B. Bhattacharya, Nonergodicity of the Nose-Hoover chain thermostat in computationally achievable time, *Phys. Rev. E* **90** (4) (2014) 043304.
- [53] M.S. Daw, S.M. Foiles, M.I. Baskes, The embedded-atom method: a review of theory and applications, *Mater. Sci. Rep.* **9** (7–8) (1993) 251–310.
- [54] D. Utt, A. Stukowski, K. Albe, Grain boundary structure and mobility in high-entropy alloys: A comparative molecular dynamics study on a Σ11 symmetrical tilt grain boundary in face-centered cubic CuNiCoFe, *Acta Mater.* **186** (2020) 11–19.
- [55] D.Q. Doan, T.H. Fang, T.H. Chen, Influences of grain size and temperature on tribological characteristics of CuAlNi alloys under nanoindentation and nanoscratch, *Int. J. Mech. Sci.* **185** (2020) 105865.
- [56] X.W. Zhou, R.A. Johnson, H.N.G. Wadley, Misfit-energy-increasing dislocations in vapor-deposited CoFe/NiFe multilayers, *Phys. Rev. B* **69** (14) (2004) 144113.
- [57] Z. Lin, R.A. Johnson, L.V. Zhigilei, Computational study of the generation of crystal defects in a bcc metal target irradiated by short laser pulses, *Phys. Rev. B* **77** (21) (2008) 214108.
- [58] J. Li, Q. Fang, B. Liu, Y. Liu, Y. Liu, Mechanical behaviors of AlCrFeCuNi high-entropy alloys under uniaxial tension via molecular dynamics simulation, *RSC Adv.* **6** (80) (2016) 76409–76419.
- [59] J. Li, Q. Fang, B. Liu, Y. Liu, Y. Liu, Atomic-scale analysis of nanoindentation behavior of high-entropy alloy, *J. Micromech. Mol. Phys.* **1** (01) (2016) 1650001.
- [60] S. Zhang, Y. Xu, X. Liu, S.N. Luo, Competing roles of interfaces and matrix grain size in the deformation and failure of polycrystalline Cu-graphene nanolayered composites under shear loading, *Phys. Chem. Chem. Phys.* **20** (36) (2018) 23694–23701.
- [61] J. Schiøtz, F.D. Di Tolla, K.W. Jacobsen, Softening of nanocrystalline metals at very small grain sizes, *Nature* **391** (6667) (1998) 561–563.
- [62] M.I. Mendelson, Average grain size in polycrystalline ceramics, *J. Am. Ceram. Soc.* **52** (8) (1969) 443–446.
- [63] A.V. Pham, T.H. Fang, A.S. Tran, T.H. Chen, Structural and mechanical characterization of sputtered CuNi100-x thin film using molecular dynamics, *J. Phys. Chem. Solids* **147** (2020) 109663.
- [64] J.D. Honeycutt, H.C. Andersen, Molecular dynamics study of melting and freezing of small Lennard-Jones clusters, *J. Phys. Chem.* **91** (19) (1987) 4950–4963.
- [65] Y. Qi, H. Xu, T. He, M. Wang, M. Feng, Atomistic simulation of deformation behaviors polycrystalline CoCrFeMnNi high-entropy alloy under uniaxial loading, *Int. J. Refract. Met. Hard Mater.* **95** (2021) 105415.
- [66] Z. Wang, J. Li, Q. Fang, B. Liu, L. Zhang, Investigation into nanoscratching mechanical response of AlCrFeCuNi high-entropy alloys using atomic simulations, *Appl. Surf. Sci.* **416** (2017) 470–481.
- [67] A. Stukowski, Visualization and analysis of atomistic simulation data with OVITO—the Open Visualization Tool, *Model. Simul. Mater. Sci. Eng.* **18** (1) (2009) 015012.
- [68] T.D. Le, R. Noumeir, H.L. Quach, J.H. Kim, J.H. Kim, Critical temperature prediction for a superconductor: A variational bayesian neural network approach, *IEEE Trans. Appl. Supercond.* **30** (4) (2020) 1–5.
- [69] J.F. Masson, J.S. Biggins, E. Ringe, Machine learning for nanoplasmonics, *Nat. Nanotechnol.* **18** (2) (2023) 111–123.
- [70] D.C. Montgomery, E.A. Peck, G.G. Vining, Introduction to linear regression analysis, John Wiley & Sons, 2021.
- [71] S.R. Gunn, Support vector machines for classification and regression, *ISIS Tech. Rep.* **14** (1) (1998) 5–16.
- [72] J.H. Friedman, Greedy function approximation: a gradient boosting machine, *Ann. Stat.* (2001) 1189–1232.
- [73] Y. LeCun, Y. Bengio, G. Hinton, Deep learning, *nature* **521** (7553) (2015) 436–444.

- [74] Albawi, S., Mohammed, T.A., & Al-Zawi, S. (2017, August). Understanding of a convolutional neural network. In *2017 International Conference on Engineering and Technology (ICET)* (pp. 1-6). Ieee.
- [75] Z. Li, F. Liu, W. Yang, S. Peng, J. Zhou, A survey of convolutional neural networks: analysis, applications, and prospects, *IEEE Trans. Neural Netw. Learn. Syst.* (2021).
- [76] S. Hochreiter, J. Schmidhuber, Long short-term memory, *Neural Comput.* 9 (8) (1997) 1735–1780.
- [77] Y. Yu, X. Si, C. Hu, J. Zhang, A review of recurrent neural networks: LSTM cells and network architectures, *Neural Comput.* 31 (7) (2019) 1235–1270.
- [78] Y. Qi, T. He, H. Xu, Y. Hu, M. Wang, M. Feng, Effects of microstructure and temperature on the mechanical properties of nanocrystalline CoCrFeMnNi high entropy alloy under nanoscratching using molecular dynamics simulation, *J. Alloy. Compd.* 871 (2021) 159516.
- [79] L. Li, Q. Fang, J. Li, B. Liu, Y. Liu, P.K. Liaw, Lattice-distortion dependent yield strength in high entropy alloys, *Mater. Sci. Eng.: A* 784 (2020) 139323.
- [80] X. Du, X. Lu, S. Shuang, Z. Wang, Q.L. Xiong, G. Kang, X. Zhang, Cyclic plasticity of CoCrFeMnNi high-entropy alloy (HEA): A molecular dynamics simulation, *Int. J. Appl. Mech.* 13 (01) (2021) 2150006.
- [81] A. Sharma, G. Balasubramanian, Dislocation dynamics in Al0.1CoCrFeNi high-entropy alloy under tensile loading, *Intermetallics* 91 (2017) 31–34.
- [82] L. Xie, G. Wu, P.K. Liaw, W. Wang, D. Li, Q. Peng, Y. Zhang, Temperature gradient enhances the solidification process and properties of a CoCrFeNi high-entropy alloy: Atomic insights from molecular dynamics simulations, *Comput. Mater. Sci.* 231 (2024) 112538.
- [83] Z. Fu, W. Chen, H. Wen, D. Zhang, Z. Chen, B. Zheng, E.J. Lavernia, Microstructure and strengthening mechanisms in an FCC structured single-phase nanocrystalline Co25Ni25Fe25Al7.5Cu17.5 high-entropy alloy, *Acta Mater.* 107 (2016) 59–71.
- [84] Q. Fang, Y. Chen, J. Li, C. Jiang, B. Liu, Y. Liu, P.K. Liaw, Probing the phase transformation and dislocation evolution in dual-phase high-entropy alloys, *Int. J. Plast.* 114 (2019) 161–173.



Hoang-Giang Nguyen is a lecturer in the Faculty of Engineering and Technology at Kien Giang University. He received his Ph.D. in Mechanical Engineering at the National Kaohsiung University of Science and Technology between 2021 and 2024. Throughout his doctoral studies, he authored multiple articles in respected peer-reviewed journals such as JALCOM, IJMS, MSE, and IJP postgraduate studies, employing a hybrid approach that integrates molecular dynamic simulation and machine learning methods. Additionally, his work encompasses computational modeling principles, nanotechnology, mechanical properties, mechanics, machine vision, and machine learning techniques, all aimed at designing and forecasting the mechanical properties of novel materials with applications in energy and intelligent control systems.



Thanh-Dung Le (Member, IEEE) received a B.Eng. degree in mechatronics engineering from Can Tho University, Vietnam, an M.Eng. degree in electrical engineering from Jeju National University, S. Korea, and a Ph.D. in electrical engineering from Ecole de Technologie Supérieure (ETS), University of Quebec, Canada. Currently, he is a postdoctoral fellow at the Biomedical Information Processing Laboratory, ETS. His research interests include applied machine learning approaches for critical decision-making systems. Before that, he joined the Institut National de la Recherche Scientifique, Canada, where he researched classification theory and machine learning. He received the merit doctoral scholarship from Le Fonds de Recherche du Québec Nature et Technologies. He also received the NSERC-PERSWADe fellowship in Canada and a graduate scholarship from the Korean National Research Foundation, S. Korea.



Hong-Giang Nguyen received a B.Eng. degree in Math and Information from Hue University, Vietnam, an M.B.A. degree in business administration from Hue University, Viet Nam, and a Ph.D. in Civil Engineering from National Kaohsiung University of Science and Technology, Taiwan. Currently, he is a lecturer in the Hue University. His research interests include applied math and machine learning approaches for Civil Engineering.



Te-Hua Fang (IET Fellow, CSME Fellow, ISDS Fellow, TIKI Fellow). He received his M.S. and Ph.D. degrees in mechanical engineering from National Cheng Kung University, Tainan, in 1995 and 2000, respectively. From 2001–2005, he was an Assistant Professor and an Associate Professor at the Southern Taiwan University of Technology, Tainan. He joined the Institute of Electromechanical Engineering, National Formosa University, Yunlin, in 2005, as an Associate Professor, where he was a Full Professor in 2007. He joined the National Kaohsiung University of Science and Technology (NKUST), Kaohsiung, Taiwan, as a Full Professor, in 2010. He was Head of the Department of Mechanical Engineering (2018–2022). He is currently the Chair Professor of NKUST and Dean, College of Intelligent Mechanical and Electrical Engineering (2023 now). His current research interests include molecular simulation, mechanical characteristics, and nanotechnology. He is a Fellow of TIKI. He is also a member of ASME. He was a recipient of the Young Outstanding Award and the Outstanding Research Award from the National Science Council, Taiwan, in 2007 and 2011.